Global Variations in Oceanic Evaporation (1958–2005): The Role of the Changing Wind Speed

LISAN YU

Department of Physical Oceanography, Wood Hole Oceanographic Institution, Woods Hole, Massachusetts

(Manuscript received 4 October 2006, in final form 2 March 2007)

ABSTRACT

Global estimates of oceanic evaporation (Evp) from 1958 to 2005 have been recently developed by the Objectively Analyzed Air–Sea Fluxes (OAFlux) project at the Woods Hole Oceanographic Institution (WHOI). The nearly 50-yr time series shows that the decadal change of the global oceanic evaporation (Evp) is marked by a distinct transition from a downward trend to an upward trend around 1977–78. Since the transition, the global oceanic Evp has been up about 11 cm yr^{-1} (~10%), from a low at 103 cm yr^{-1} in 1977 to a peak at 114 cm yr^{-1} in 2003. The increase in Evp was most dramatic during the 1990s. The uncertainty of the estimates is about ±2.74 cm yr^{-1}. By utilizing the newly developed datasets of Evp and related air–sea variables, the study investigated the cause of the decadal change in oceanic Evp. The decadal differences between the 1990s and the 1970s indicates that the increase of Evp in the 1990s occurred over a global scale and had spatially coherent structures. Larger Evp is most pronounced in two key regions—one is the paths of the global western boundary currents and their extensions, and the other is the tropical Indo-Pacific warm water pools. It is also found that Evp was enlarged primarily during the hemispheric wintertime (defined as the mean of December–February for the northern oceans and June–August for the southern oceans). Despite the dominant upward tendency over the global basins, a slight reduction in Evp appeared in such regions as the subtropical centers of the Evp maxima as well as the eastern equatorial Pacific and Atlantic cold tongues.

An empirical orthogonal function (EOF) analysis was performed for the yearly winter-mean time series of Evp and the related air–sea variables [i.e., wind speed (U) and air–sea humidity differences (dq)]. The analysis suggested a dominant role of the wind forcing in the decadal change of both Evp and dq. It is hypothesized that wind impacts Evp in two ways. The first way is direct: the greater wind speed induces more evaporation by carrying water vapor away from the evaporating surface to allow the air–sea humidity gradients to be reestablished at a faster pace. The second way is indirect: the enhanced surface wind strengthens the wind-driven subtropical gyre, which in turn drives a greater heat transport by the western boundary currents, warms up SST along the paths of the currents and extensions, and causes more evaporation by enlarging the air–sea humidity gradients. The EOF analysis performed for the time series of the global annual-mean Evp fields showed that the first three EOF modes account for nearly 50% of the total variance. The mode 1 variability represents the upward trend in Evp after 1978 and is attributable to the increased U, and the mode 2 variability explains much of the downward trend in Evp before 1978 and is correlated to the global dq variability. The EOF mode 3 of Evp captures the interannual variability of Evp on time scales of the El Niño–Southern Oscillation, with the center of action over the eastern equatorial Pacific.

1. Introduction

Oceanic evaporation is the process through which water molecules change from a liquid phase to a vapor phase at the air–sea interface. The three requirements that evaporation is dependent upon are heat energy, air–sea humidity differences, and wind. Heat energy is used to break the hydrogen bonds that bind the water molecules together. Each water molecule that becomes water vapor takes a parcel of heat with it, and the energy remains latent until later to be released during the condensation process. Air humidity refers to the amount of water vapor in the air, and it needs to be lower than the humidity of the evaporating sea surface for evaporation to take place. Turbulent air movement

Corresponding author address: Lisan Yu, Department of Physical Oceanography, Woods Hole Oceanographic Institute, MS #21, Woods Hole, MA 02543.
E-mail: lyu@whoi.edu

DOI: 10.1175/2007JCLI1714.1

related to wind speed and surface roughness facilitates the evaporation because it carries water vapor away from the evaporating sea surface and helps to maintain a vertical air–sea humidity gradient.

Using the bulk parameterization and the similarity theory described by Liu et al. (1979), the rate of evaporation (Evp) can be computed from the following relation:

$$\text{Evp} = c_e U(q_s - q_a) = c_e U\, dq, \tag{1}$$

where q_s is the saturation specific humidity at the sea surface temperature (SST), q_a is the near-surface atmospheric specific humidity, dq represents the difference between q_s and q_a, U is the near-surface wind, and c_e is a turbulent exchange coefficient and is determined by the atmospheric stability, the air–sea temperature differences, and the wind speed (Fairall et al. 2003). The relationships between c_e, U, and q_a can be both local and large scale, and are influenced by SST (Cayan 1992; Zhang and McPhaden 1995). It is anticipated from Eq. (1) that Evp will change when SST changes.

Temperatures of the global oceans and atmosphere have been increasing, and the change is particularly pronounced in the past two decades from the 1980s through the 1990s (Houghton et al. 2001). One intuitive consequence of the global warming is that the moisture holding capacity of the atmosphere should go up following the Clausius–Clapeyron equation. While warmer air holds more moisture, warmer sea surface evaporates more readily. The enhanced evaporation will increase the salinity by removing water from the ocean surface and leaving salt behind. At the same time, the increased amount of water vapor will enhance the atmospheric moisture content. Recent in situ and satellite evidence indicated that these changes have indeed been occurring. For instance, Boyer et al. (2005) found from the salinity observations (1955–98) that most of the tropical and subtropical Atlantic oceans have become saltier in the upper 500 m. They speculated that these salinity changes in the shallow upper layer were forced at the surface by an increased evaporation. Their analysis was in consistency with Curry et al. (2003), who also found a salinity increase in the northern and southern subtropics of the Atlantic Ocean between the 1950s and the 1990s and estimated a 5%–10% increase in net evaporation. Meanwhile, Trenberth et al. (2005) were able to link the column-integrated water vapor (precipitable water) observations from radiosonde to those from the Special Sensor Microwave Imager (SSM/I; Wentz 1997) and deduced that atmospheric moisture amounts started to rise after about 1973 (Ross and Elliott 2001), and the upward trend was about 1.3% ± 0.3% per decade.

Despite the supporting theoretical arguments and observational evidence indicative of increased evaporation associated with the rising global temperatures, the lack of direct observations hampers the efforts to identify and quantify the change of the oceanic evaporation over the past decades. Without Evp observations, the bulk parameterization in Eq. (1) provides the only means to estimate Evp from air–sea variables (such as wind, SST, air temperature, and humidity). These variables can be either observed by ships and satellite sensors or modeled by numerical weather prediction (NWP) reanalyses such as those from the National Center for Atmospheric Research–National Centers for Environmental Prediction (NCAR–NCEP) and the 40-yr European Centre for Medium-Range Weather Forecasts (ECMWF) Re-Analysis (ERA-40). For a long time, our knowledge of global ocean evaporation has gained from climatological atlases constructed from ship-based surface meteorological reports (Bunker 1976; Esbensen and Kushnir 1981; Oberhuber 1988; da Silva et al. 1994; Josey et al. 1999). Ship measurements have good accuracy and span several decades, and the ship-based Evp atlases provide the first-order, large-scale picture of the long-term annual mean of ocean evaporation at good accuracy. However, ship measurements alone do not permit a construction of time series beyond the climatological mean, because of poor data sampling in both space and time. In regions such as the southern oceans there are literally no observations over the multidecade data-collecting period.

The NWP model reanalyses offer continuing time series from the 1950s onward with a complete global coverage, but they suffer from systematic biases in the models. The large uncertainty is a major impediment to the application of the reanalysis products to climate assessment studies. Meanwhile, satellite retrievals have good coverage and resolution and have been available since the launch of SSM/I in July 1987. Nonetheless, improving the satellite-based Evp estimates is challenged by the technical difficulty in retrieving air temperature and humidity near the sea surface. The lack of direct observations of air–sea humidity contrasts has serious effect on the accuracy of satellite Evp estimates.

Efforts have been made recently to improve estimates of latent (evaporation) heat flux (LHF) through appropriate combination of surface meteorology from in situ measurements, satellite observations, and NWP model reanalysis outputs by a project named Objectively Analyzed Air–Sea Fluxes (OAFlux; Yu et al. 2004a,b; Yu and Weller 2007). Under the auspices of the National Oceanic and Atmospheric Administration (NOAA) Office of Climate Observations (OCO) and Climate Change Data and Detection (CCDD), the

project develops the global analysis of surface flux fields for the past 50 years. Once LHF is estimated, Evp can be determined using the following relation:

$$\text{Evp} = \text{LHF}/\rho_w L_e, \quad (2)$$

where ρ_w is the density of seawater, and L_e is the latent heat of vaporization that can be expressed as $L_e = [2.501 - (0.002\,37 \times \text{SST})] \times 10^6$. By doing so, a nearly 50-yr time series of global Evp fields is derived as a by-product of the OAFlux project.

This purpose of this study is to capitalize on the availability of the state-of-the-art estimation of Evp to investigate the long-term change of the oceanic evaporation. Three issues are particularly emphasized: How much has Evp changed since the late 1950s? Where did the change occur? What caused the change? The ocean, being the source of 86% of the global evaporation and the receiver of 78% of global precipitation (Schmitt and Wijffels 1993), is a key component of the global water cycle. An evolving water cycle has an impact on everything from environmental concerns to human water demands. It is expected that the knowledge gained from this study will help to gauge a better understanding of the climate behavior of the water cycle in the context of global climate change.

The paper is organized as follows. A brief description of the Evp estimates and the mean annual patterns is given in section 2. The long-term change in Evp is shown in section 3, followed by the analysis of the cause of the change in section 4. Summary and conclusions are included in section 5.

2. Data and the basic mean patterns

a. Data description

Daily estimates of the global LHF fields on a one-degree grid have been produced by the OAFlux project for the period from 1958 to the present. The time series of Evp used in the study was computed from Eq. (1) based on daily LHF estimates. The OAFlux LHF product is different from other flux products in that it is not constructed from one single data source, but rather it is determined by objectively blending the data sources from satellite and NWP model outputs while using in situ observations to assign the weights (Yu et al. 2004a; Yu and Weller 2007). The methodology of the objective analysis is based on the Gauss–Markov theorem, a standard statistical estimation theory that states, when combining data in a linear fashion, that the linear least squares estimator is the most efficient estimator, and such a process reduces error in each input data source and produces an estimate that has the minimum variance (Daley 1991). In case of the flux estimation, the objective analysis allows us to formulate a least squares problem based on the input datasets to be used and to search for a solution that best fits to the input datasets. The formulation is applied to each of the flux-related surface meteorological variables (i.e., wind speed, specific air humidity, air temperature, and sea surface temperature), and the variable values at the solution form the base for computing LHF from the Coupled Ocean–Atmosphere Response Experiment (COARE) bulk flux algorithm 3.0 (Fairall et al. 1996; Bradley et al. 2000).

The input datasets for synthesis included satellite SST retrievals from the Advanced Very High Resolution Radiometer (AVHRR), the Tropical Rainfall Measuring Mission (TRMM) Microwave Imager (TMI) and Advanced Microwave Scanning Radiometer for the Earth Observing System (EOS; AMSR-E; Chelton and Wentz 2005), wind speed retrievals from SSM/I (Wentz 1997), ocean surface vector wind retrievals from the Quick Scatterometer (QuikSCAT), the optimum interpolation (OI) 1/4-degree daily SST analysis of Reynolds et al. (2007), surface meteorology from the reanalysis/forecast models of the ECMWF (Uppala et al. 2005) and NCAR–NCEP (Kalnay et al. 1996; Kanamitsu et al. 2000), and ship reports from the Comprehensive Ocean–Atmosphere Data Set (COADS). The resulting LHF fields were evaluated using more than 100 flux buoy measurements that are available over the global oceans (Yu et al. 2004b), including those acquired by the Woods Hole Oceanographic Institution (WHOI) Upper Ocean Processes group (e.g., Moyer and Weller 1997) and from the Pilot Research Moored Array in the Tropical Atlantic (PIRATA; Servain et al. 1998) and the Tropical Atmosphere Ocean/Triangle Trans-Ocean Buoy Network (TAO/TRITON) array in the equatorial Pacific (McPhaden et al. 1998). Overall, the OAFlux estimates of LHF differ from the measured fluxes by 3–8 W m^{-2} (~2%–8%) across the measurement locations, while the two NWP fluxes are overestimated by 18–20 W m^{-2} (>15%). For detailed information about the synthesis procedure and the data products, the readers are invited to visit the project Web site (at http://oaflux.whoi.edu) or refer to the studies by Yu and Weller (2007).

b. Annual and seasonal mean climatology

The annual-mean Evp climatology averaged over the period 1958–2005 (Fig. 1a) shows that the global Evp distribution is roughly zonally oriented, with larger Evp (>180 cm yr^{-1}) occurring over the subtropical latitudes of the global oceans and smaller Evp (<60 cm yr^{-1}) over the equatorial cold tongues and higher northern

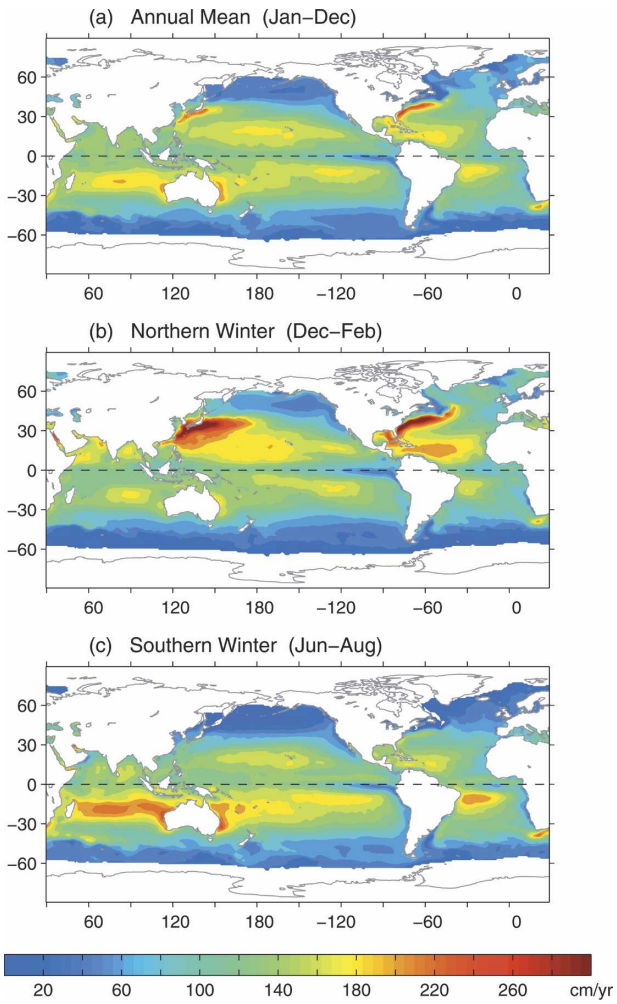

FIG. 1. Mean global Evp pattern for (a) the annual average, (b) the northern winter average (December–March), and (c) the austral winter average (June–September). The averages are constructed from the 1958–2005 base period.

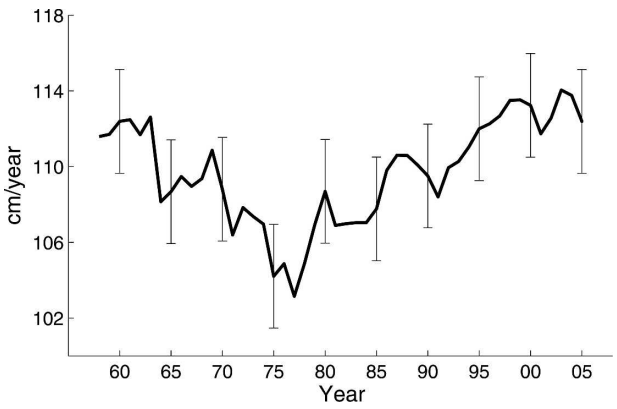

FIG. 2. Variations of the yearly mean Evp averaged over the global ice-free oceans. The error bars indicate 1 std dev from the 1958–2005 mean.

and southern latitudes. Exceptions to this zonal pattern are the regions of the western boundary currents (WBCs) and their extensions, where Evp is enhanced considerably along the pathways of the WBCs. These WBC regions include the Gulf Stream off the United States, the Kuroshio and Kuroshio Extension off Japan, the eastern Australian Current, the Agulhas Current off the African coast, and the Falkland/Brazilian Current off South America.

Seasonally, wind speed and air–sea humidity and temperature differences are at their maximum strength in the fall and winter. It is evident that Evp in the Northern (Southern) Hemisphere is intensified considerably during the boreal (austral) wintertime. Such winter intensification is most pronounced over the regions of the Gulf Stream and Kuroshio and their extensions (Figs. 1b–c), where the magnitude of Evp exceeds 300 cm yr^{-1} in the boreal winter but is less than 100 cm yr^{-1} in the boreal summer. Among the five above-mentioned WBC regions, the seasonal change in Evp is weakest over the Falkland/Brazilian Current off South America. The reason is that the landmass of South America is relatively narrow and terminates at the mid-latitudes, and so the air from the continent is less cold and dry compared to the air advected by strong westerlies off eastern North America and Asia.

In general, the annual-mean Evp pattern is dominated by the winter pattern of each hemisphere. On the annual basis, large Evp concentrates mostly over the subtropical oceans and along the WBCs and their extensions. The pattern of annual variability is in good consistency with ship-based Evp climatologies (Bunker 1976; Esbensen and Kushnir 1981; Oberhuber 1988; da Silva et al. 1994; Josey et al. 1999).

3. Variability of Evp during 1958–2005

The data record covers 48 complete years from 1958 to 2005. To identify the pattern of change during this period, the time series of the yearly mean Evp averaged over the global ice-free oceans is constructed (Fig. 2). Error bars of 2.74 cm yr^{-1}, which represent one standard deviation from the 48-yr mean, are placed on the Evp time series. Interestingly, the change of Evp is marked by a distinct transition from a downward trend to an upward trend around 1977–78. The time of the transition coincided with the occurrence of a major climate shift that has been reported by many studies (Trenberth 1990; Mantua et al. 1997). Cayan (1992) also noted a change in latent and sensible heat fluxes. Since then the global oceanic Evp has been up about

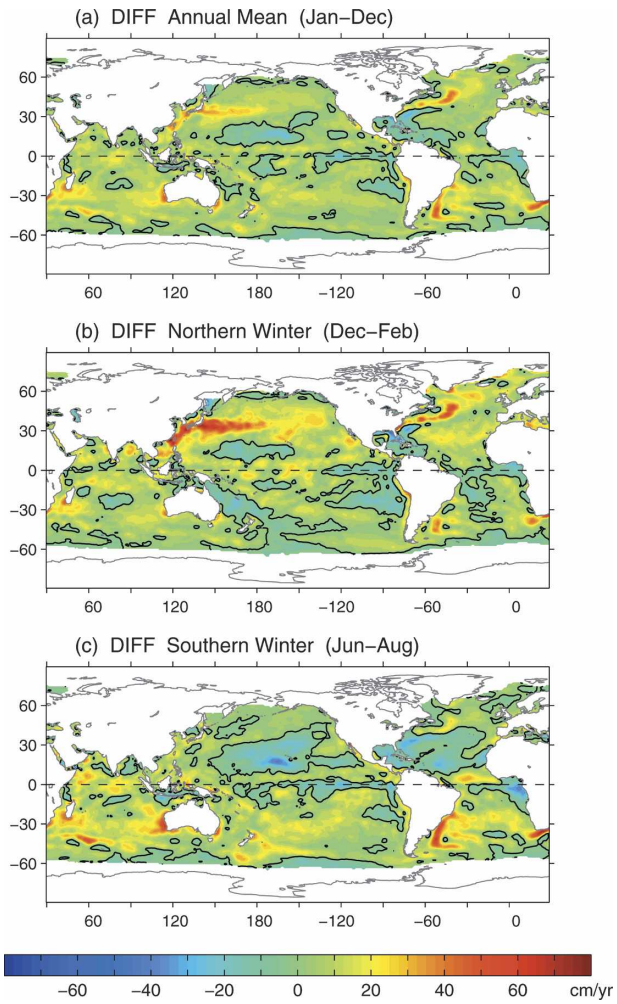

FIG. 3. Evp differences between the 1990s and the 1970s in (a) annual mean, (b) northern winter (December–February), and (c) southern summer (June–August). Zero contours are shown by thin black lines.

11 cm yr^{-1} (~10%), from a low at 103 cm yr^{-1} in 1977 to a peak at 114 cm yr^{-1} in 2003. The upward trend was most intense during the 1990s; after that the trend has been weak and was interrupted by a significant reduction in 2002.

Mean Evp fields are computed for two periods: one is the decade of a fast increase represented by the years 1990–98, and the other is the decade of a fast decrease represented by the years 1970–78. The two mean fields are subtracted and the differences are shown in Fig. 3a. Interestingly, the difference map shows that the changes between the two decades not only occur over a global scale but also have a large-scale coherence pattern—the latter is most evident when paired with the climatological annual-mean pattern in Fig. 1a. The change in the following three structures is most outstanding. The first structure is the large Evp over the subtropics, where, on the annual basis, a center of maximum is located at 10°–20° northern and southern latitudes in each basin. These centers of maximum, however, became slightly reduced in the 1990s when Evp over most global oceans enhanced. The second structure is the large Evp along the WBC and extension regions of the global oceans. The increase of Evp over these regions is most pronounced. The third is the Evp in the tropical oceans. Climatologically, Evp is larger over the tropical Indo-Pacific warm pools and smaller over the eastern equatorial Pacific and Atlantic cold tongues. The changes made in the 1990s, more Evp over the warm pools and less Evp over the cold tongues, further enlarge the contrast between the two regions of different water temperatures.

The Evp annual-mean pattern is seasonally dependent, with stronger Evp in the hemispheric winter when temperature gradients and land/sea contrasts are strongest. When differentiating the boreal winter (December–February) from the austral winter (June–August) in making the difference plots, the enhancement of Evp for each hemisphere took place primarily during the hemispheric winter. The northern Pacific and Atlantic Oceans are a clear example, where the difference anomalies are large and positive in the winter but are small and negative in the summer. The seasonal contrast is, however, less obvious in the Indian Ocean where the increase of Evp occurred in all seasons, albeit being amplified slightly in the austral wintertime.

4. Cause of the change in Evp

From Eq. (1), a changing Evp reflects a change in either wind speed (U), or air–sea humidity differences (dq), or both. Which variable is most responsible? As Evp for each hemisphere is enhanced mostly during the hemispheric wintertime, the analysis begins with the North Pacific and Atlantic basins in the boreal winter, followed by the southern oceans in the austral winter, and ends with an integrated view of the global annual-mean field.

a. The North Atlantic and Pacific Oceans in the boreal winter

Figure 4a provides a close look at the differences of the winter Evp between the decades of the 1970s and 1990s for the North Pacific and Atlantic Oceans. Large positive anomalies are centered over the Kuroshio and the Gulf Stream; yet the zonal and meridional extent of the anomalies stretches out far beyond the extension

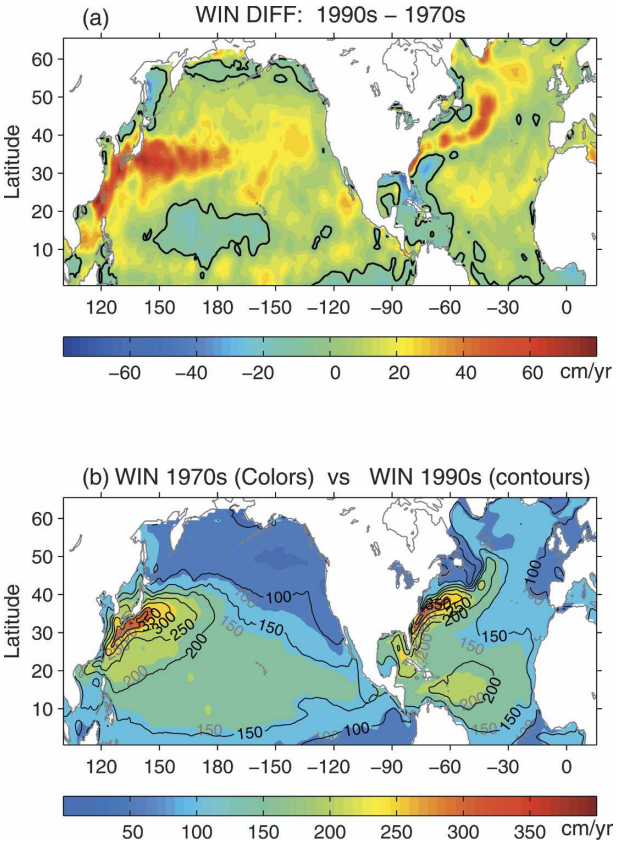

FIG. 4. (a) Evp differences between the 1990s and the 1970s. Zero contours are indicated by black lines. (b) Mean Evp pattern in the 1990s (black contours) superimposed with the mean pattern in the 1970s (colors).

regions of the two current systems. To identify the cause of the anomaly pattern, the mean Evp field of the 1990s is superimposed onto the mean field of the 1970s (Fig. 4b). It is evident that the positive anomalies are the result of the intensification and northward and eastward expansion of the large Evp center associated with the Kuroshio and the Gulf Stream. In the Atlantic Ocean, the core Evp center in the 1990s had a slight northward shift compared to that in the 1970s, leading to a reduced Evp in the south over the Gulf of Mexico.

Here, U and dq are the two key variables that are directly related to Evp. As the large-scale near-surface wind circulation is governed by the sea level pressure (SLP) system, a better understanding can be obtained by analyzing the change of wind in the context of the SLP pattern change. Climatologically, the winter SLP fields in the two basins are all dictated by strong low SLP in the north, named the Aleutian low in the Pacific and the Icelandic low in the Atlantic, and strong high SLP to the south (Fig. 5a). The lows direct anticlockwise circulation and the highs clockwise circulation, funneling a strong westerly jet stream within the midlatitudes 30°–50°N. To the south, broad easterlies dominate. The decadal change in SLP (Fig. 5b) is most striking with regard to the strengthening and deepening southward of the low pressure systems (Hurrell 1995; Nakamura et al. 1997). The Aleutian low SLP was about 4 mb lower and the Icelandic low SLP was about 3 mb lower between the 1990s and the 1970s. As the result, the westerlies associated with the two low systems strengthened and expanded southward (Fig. 5c), leading to an increase of wind speed over much of the region north of 30°N. South of the latitude, the wind speed in the central and eastern subtropical Pacific Ocean became weaker, while the wind speed in the subtropical Atlantic Ocean strengthened with the anomaly maximum located between 20°–30°N. The latter change was related to the anomalous high SLP across the subtropical Atlantic.

Compared with the decadal difference map of Evp (Fig. 4a), the wind speed was responsible for much of the Evp change in the interior ocean but not near the western boundary. In fact, the larger Evp anomalies near the western boundary in both the Pacific and Atlantic Oceans were caused by the enlarged dq anomalies. Figure 6a shows that outside of the tropics dq generally decreases with increasing latitude in the boreal winter. Stronger dq is located along the WBCs and the northward and eastward extensions resulting from the sharp land–sea contrasts. The change of dq in the 1990s was basin-scale, with large positive anomalies located over the WBCs. A slight northward shift of the large dq is seen in the Gulf Stream, which led to positive anomalies along the pathway and negative anomalies to the south over the Gulf of Mexico.

The air–sea humidity difference dq is a function of SST that can be expressed as $dq = q_s(\mathrm{SST}) - q_a(\mathrm{SST} + \Delta T)$, where ΔT is the air–sea temperature differences. The SST differences between the winters of the two decades (Fig. 6c) indicate that the enlargement of dq near the western boundary and along the WBC pathways was controlled primarily by the increased SST. However, the correlation between dq and SST is less linear in the interior ocean away from the boundaries, indicative of the influence of the atmospheric circulation on dq.

Large Evp anomalies along the western boundaries were caused by dq, while those Evp anomalies in the interior oceans were induced by U. This raises an interesting question as to whether the two sets of anomalies were induced by the same forcing. To answer this question, the analysis based on empirical orthogonal functions (EOFs) was performed for the three fields, Evp, U, and dq, respectively, using the yearly winter-

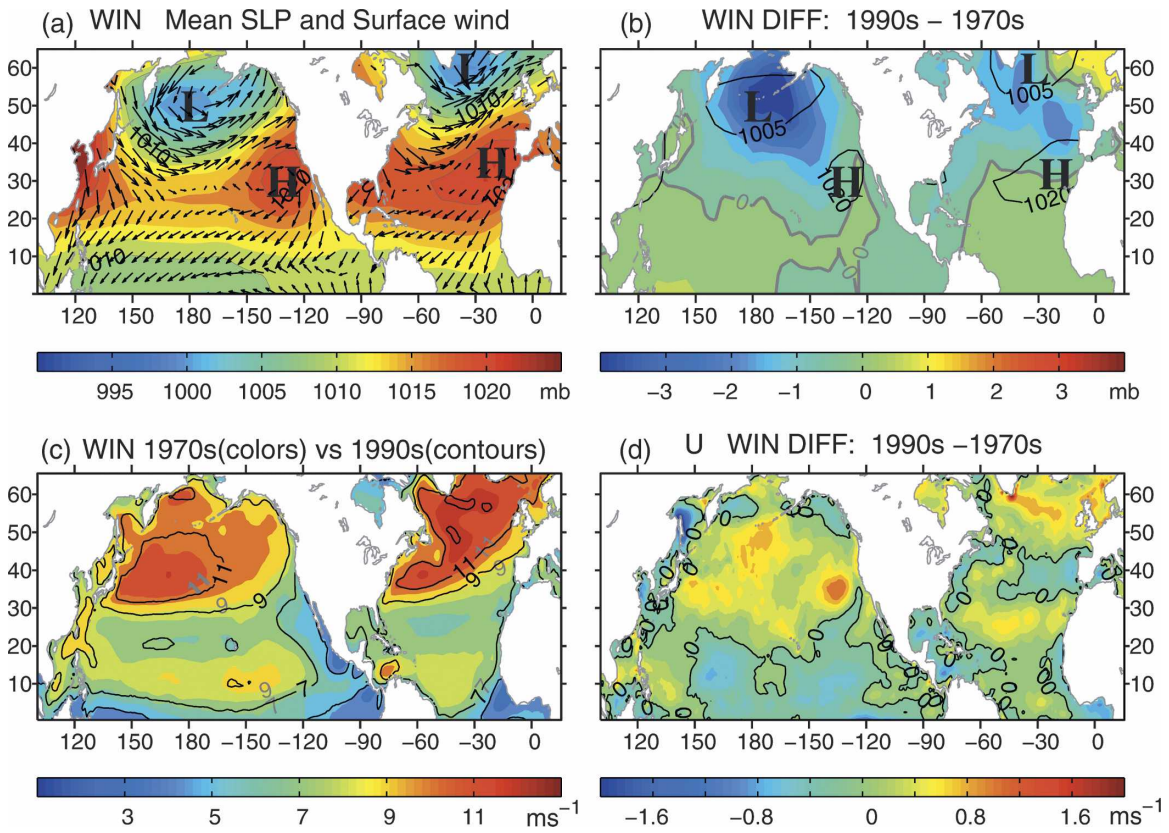

FIG. 5. (a) Climatological-mean SLP (color shaded) and surface wind (vector field) in the northern winter (December–February). (b) Differences between SLP winter pattern in the 1990s and the 1970s. Zero contours are marked by thick gray lines. The mean locations of high and low SLP centers are superimposed. (c) Mean wind speed pattern in the 1990s (black contours) superimposed with the mean pattern in the 1970s (colors). (d) Differences between the two mean wind speed patterns. Zero contours are marked by black lines.

mean time series for the period 1958–2005. The EOF analysis identifies the dominant spatial and temporal patterns in the time series. Figures 7a–c present the first EOF mode pattern for each of the three variables. These first modes capture the dominant structure of the decadal changes between the 1990s and the 1970s (see Figs. 4a, 5d, and 6c). However, the real surprise of the EOF analysis is the revelation that the three principal component (PC) time series all increase monotonically with time. The upward trends in the three PCs, though starting at different time in the 1970s, are coherent after 1980.

The coherent upward trends in the three PCs suggest that the dominant mode variability in Evp, U, and dq was induced by the same forcing. So, what was the forcing? Fig. 8a plots the time series of yearly winter (December–February) means of U averaged over the North Pacific and Atlantic Oceans. Surprisingly, the upward tendency of the three PCs resembles closely the increased year-to-year variability of U. This implies that the decadal anomalies of dq, though having a pattern different from that of U, were driven by the variability of the wind field. How could this be possible?

b. *Effects of increased wind on Evp*

The largest decadal change in dq occurred near the western boundary regions associated with the decadal increase in the SST of the Kuroshio and the Gulf Stream (Fig. 6c), indicating that the sea surface warming increased air–sea humidity contrasts and hence, Evp. In other words, the change in Evp was not the cause of the SST change but a result. So, what caused the positive anomalies of the SST along the Kuroshio and the Gulf Stream? The likely candidate is the heat transports of the WBCs in connection with the wind-driven gyre circulation. The increased winds would intensify the wind-driven oceanic gyre circulation, increasing the poleward heat transports carried by the WBCs and, subsequently, warming up the upper layer of the WBCs. Supporting evidence can be found from the study of Kelly and Dong (2004), which shows the

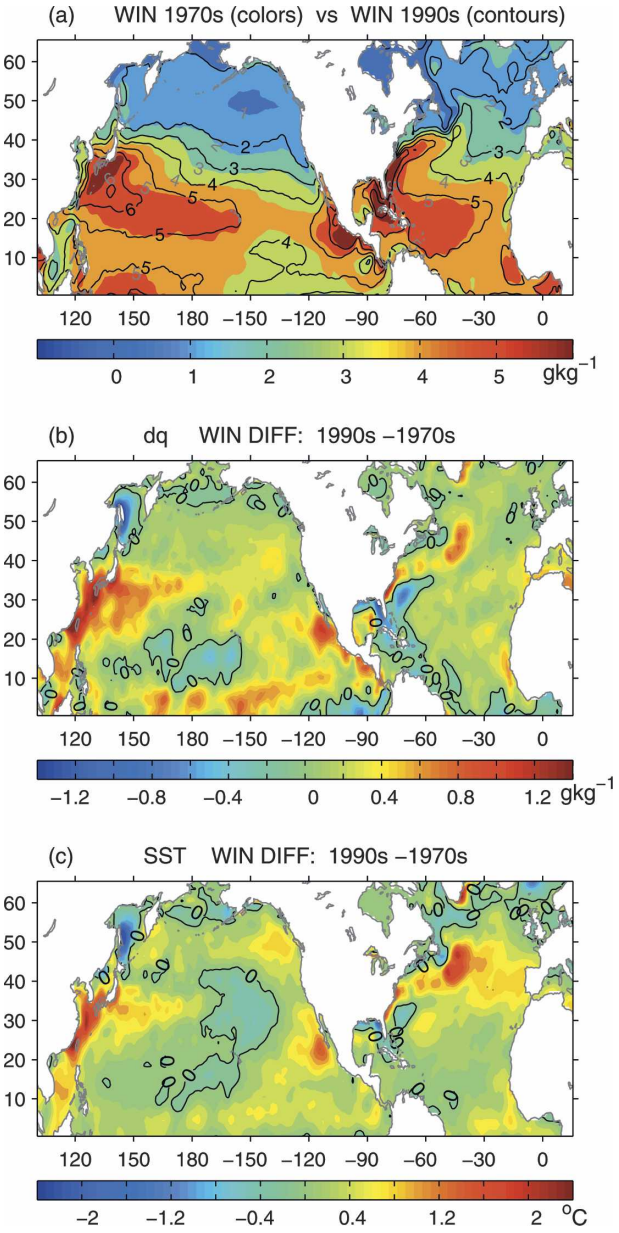

FIG. 6. (a) Mean *dq* pattern in the 1990s (black contours) superimposed with the mean *dq* pattern in the 1970s (colors). (b) Differences between the two mean *dq* patterns. (c) Differences between the mean SST pattern in the 1990s and that in the 1970s. Zeros contours in (b) and (c) are marked by black lines.

correlation of strong westerlies with positive heat content anomalies in the WBC regions.

In summary, the study proposes that winds can impact Evp by two ways. The first impact is via *U* and affects Evp in the open ocean directly under the wind anomalies. By comparison, the second impact is via SST (and hence *dq*), resulting from the intensification of the wind-driven circulation and the heat transport carried by the WBCs; and the effect is most pronounced along the WBC pathways and the extension regions. A stronger subtropical gyre in association with greater wind forcing after the Northern Hemispheric regime shift of 1976 has been reported. For instance, Qiu and Joyce (1992) indicated an increase in Kuroshio geostrophic transport of about 10 Sv [1 Sverdrup (Sv) $\equiv 10^6$ m^3 s^{-1}] for the period after the regime shift compared to the period before. Bingham (1992) reported that the subtropical gyre during 1978–82 was stronger than that during 1938–42. Miller et al. (1998) and Deser et al. (1999) indicated that the enhancement of the Kuroshio was part of a general North Pacific response to the wind shift. For the Southern Hemisphere, a decadal spinup of the wind-driven gyre in the subtropical South Pacific has also been documented in a recent study (Roemmich et al. 2007) using Argo profile and trajectory data along with altimetric height and World Ocean Circulation Experiment/Climate Variability and Predictability (WOCE/CLIVAR) hydrography. The study suggested that the greater wind forcing was associated with an increase in the Southern Hemisphere annular mode (SAM) in the 1990s.

c. *The southern oceans in the austral wintertime*

Indeed, the winds in the southern oceans have been accelerating. Figure 8b plots the year-to-year variations of *U* averaged over the austral winter season (June–August) and over the entire south oceans. A large increase of *U* in the 1990s is clearly shown. It is apparent from Figs. 8a–b that there was coherent strengthening of the near-surface wind over the global oceans after the late 1970s.

Similar to the analysis performed for the North Pacific and Atlantic Oceans, the first EOF mode was extracted from each of the three austral winter-mean time series constructed for the southern oceans (Fig. 9). It is not surprising that the three PC time series are all dictated by upward trends. The trends resemble the increased variability of yearly austral winter means of *U* in the southern oceans (Fig. 8b), suggesting, again, the importance of wind forcing. Furthermore, the enhanced Evp over the boundary currents (e.g., the Leeuwin Current, the eastern Australian Current, the Falkland/Brazilian Current, and the Agulhas Current) was caused by the positive *dq* anomalies, while the change of Evp over the open oceans was more related to the *U* anomalies. These results bear great similarity to the findings for the northern oceans (Fig. 7), further underlining that the increased winds could affect Evp through both the wind speed and the wind-driven gyre circula-

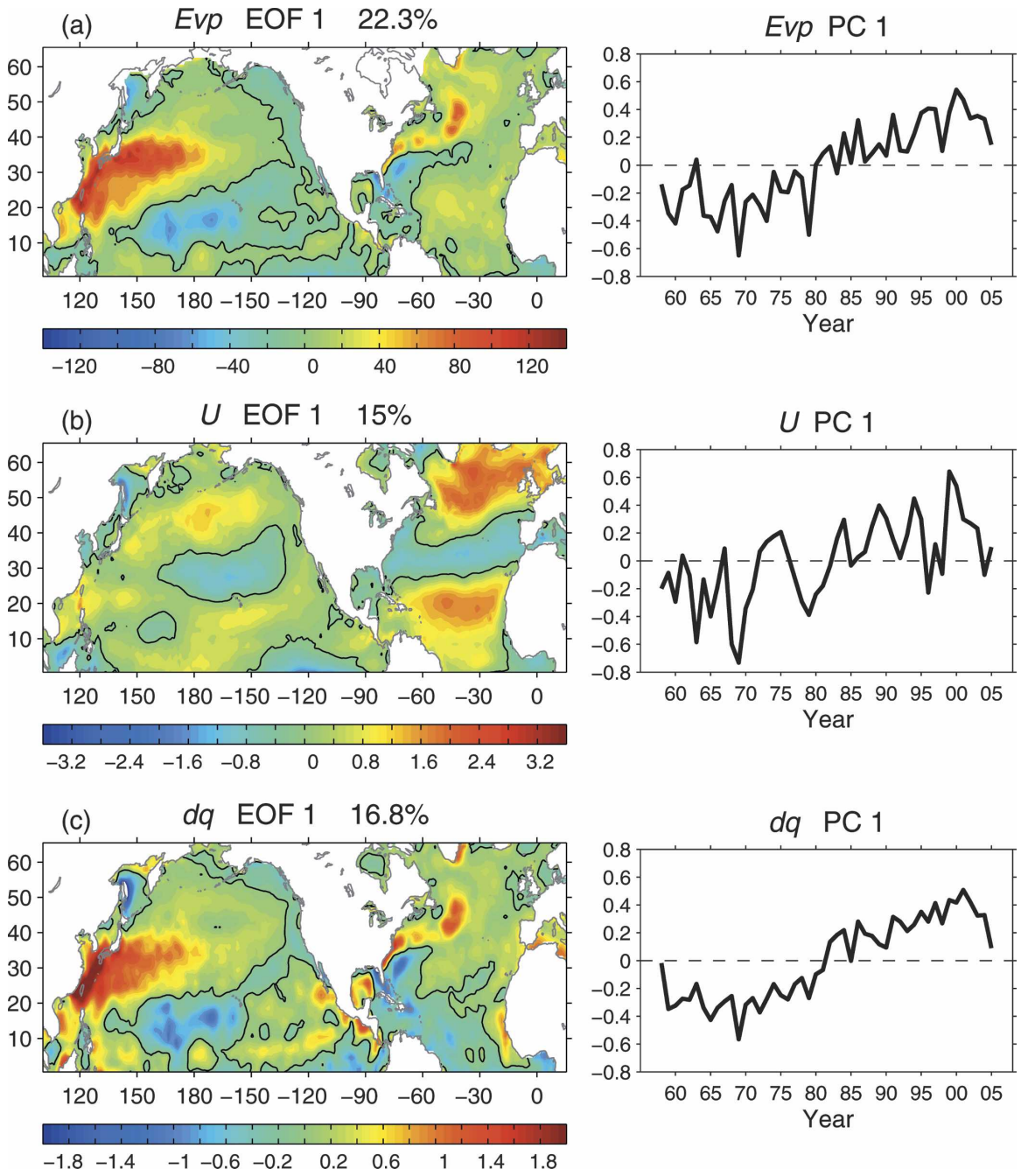

FIG. 7. (left) Pattern and (right) time series of the principal component of the EOF mode 1 based on yearly winter-mean (December–February) (a) Evp, (b) *U*, and (c) *dq* for the period of 1958–2005. Zeros contours are marked by black lines.

tion—the latter had a major impact on Evp along the paths of the boundary currents and extensions.

d. The global EOF patterns

To provide a coherent view of the change in the global Evp, the EOF analysis was performed for the time series of the annual-mean Evp fields. The first three modes of dominant Evp variability, which together explain nearly 50% of the total variance, are presented in Figs. 10a–c. The first EOF mode (Fig. 10a) represents the decadal enhancement of Evp over the global oceans. The PC time series represents primarily the increased Evp variability after 1980, which is well linked to the variability of the yearly time series of the

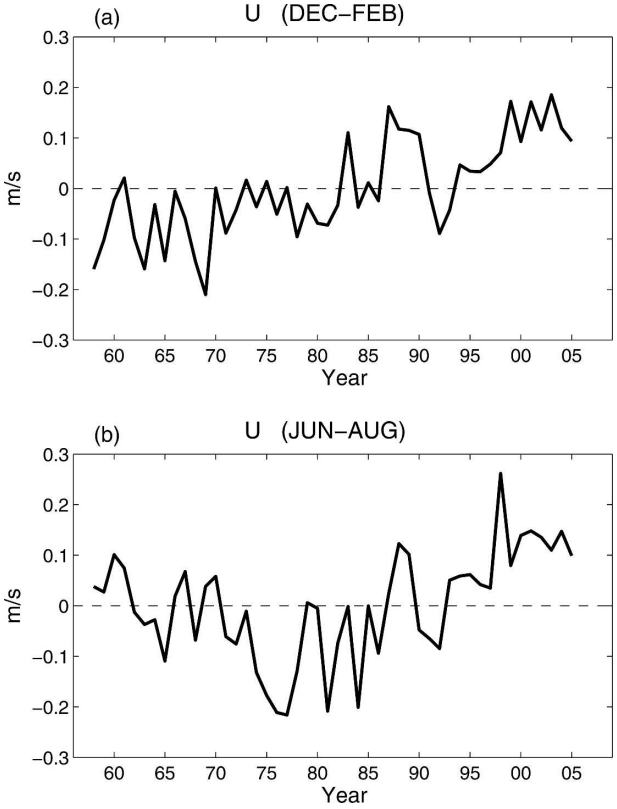

FIG. 8. Time series of (a) U averaged over the yearly boreal winter mean (December–February) for the North Pacific and Atlantic Oceans, and (b) U averaged over the yearly austral winter mean (June–August) for the southern oceans.

global U (Fig. 11a). The pattern and decadal variability of this mode are consistent with those of the first mode of Evp for each winter hemisphere (Figs. 7 and 9), suggestive of the predominant role of a changing wind in the decadal variations of Evp.

The second EOF mode of Evp (Fig. 10b) represents largely the Evp change over the global boundary regions, and the PC time series shows that the EOF mode 2 explains much of the decreased Evp variability before 1977–78. Interestingly, the PC variability of the second mode has a good agreement with the variability of the yearly time series of the global dq (Fig. 11b). This indicates that the contribution from dq is also important, though it is to a lesser degree than U. The most striking in the two EOF patterns is the contrast between boundary regions that the first mode pattern emphasizes and the ocean interior that the second mode pattern represents. The EOF1 pattern shows the regions under the direct influence of U, which further suggests that the change of dq over the WBCs is indeed induced by wind forcing. This is inconsistent with the analysis of Figs. 7 and 9 that the increased winds affect the wind-driven gyre circulation, and the latter imposes major impact on Evp along the paths of the boundary currents and extensions.

The third EOF mode of Evp (Fig. 10c) represents the interannual variability of Evp on time scales of El Niño–Southern Oscillation (ENSO), with the center of action primarily located in the eastern equatorial Pacific. Sufficient variances also appear in the eastern tropical Indian Ocean and the South Pacific convergence zone, where the regional variability on interannual time scales is closely coupled with ENSO variability (Barnett 1984; Vincent 1994).

5. Summary and discussion

A new time series of Evp (1958–2005) derived from a recent OAFlux project at WHOI shows that the decadal change of the global oceanic Evp is marked by a distinct transition from a downward trend to an upward trend around 1977–78, at the time the occurrence of a major climate shift was documented. Since the transition the global Evp has been up about 11 cm yr^{-1} ($\sim$10%), from a low at 103 cm yr^{-1} in 1977 to a peak at 114 cm yr^{-1} in 2003. The uncertainty of the estimates is about 2.74 cm yr^{-1}. The upward tendency was most intense during the 1990s.

The study utilized the new dataset of Evp and related physical variables at the air–sea interface to investigate the change of Evp over the global oceans and the cause of the change. The decadal differences between the 1990s and the 1970s indicate that the enhancement of Evp in the 1990s occurred over a global scale with spatially coherent structures. Three structural changes are most noteworthy. The first one is the change of the large Evp over the subtropics, where, on the annual basis, a center of maximum is located at 10°–20° northern and southern latitudes in each basin. These centers of maximum became reduced slightly in the 1990s when Evp over most global oceans were enhanced. The second change is the pronounced increase of the Evp along the paths of the global western boundary currents and their extensions. The third coherent pattern change is found in the tropical oceans, where Evp was enhanced over the Indo-Pacific warm pools but decreased over the eastern equatorial Pacific and Atlantic cold tongues.

The enhancement of Evp occurred primarily over the hemispheric wintertime (defined as the mean of December–February for the northern oceans and June–August for the southern oceans). The EOF analysis was performed for the yearly winter-mean time series of Evp, wind speed (U), and air–sea humidity differences (dq), respectively. The analysis yielded the dominant

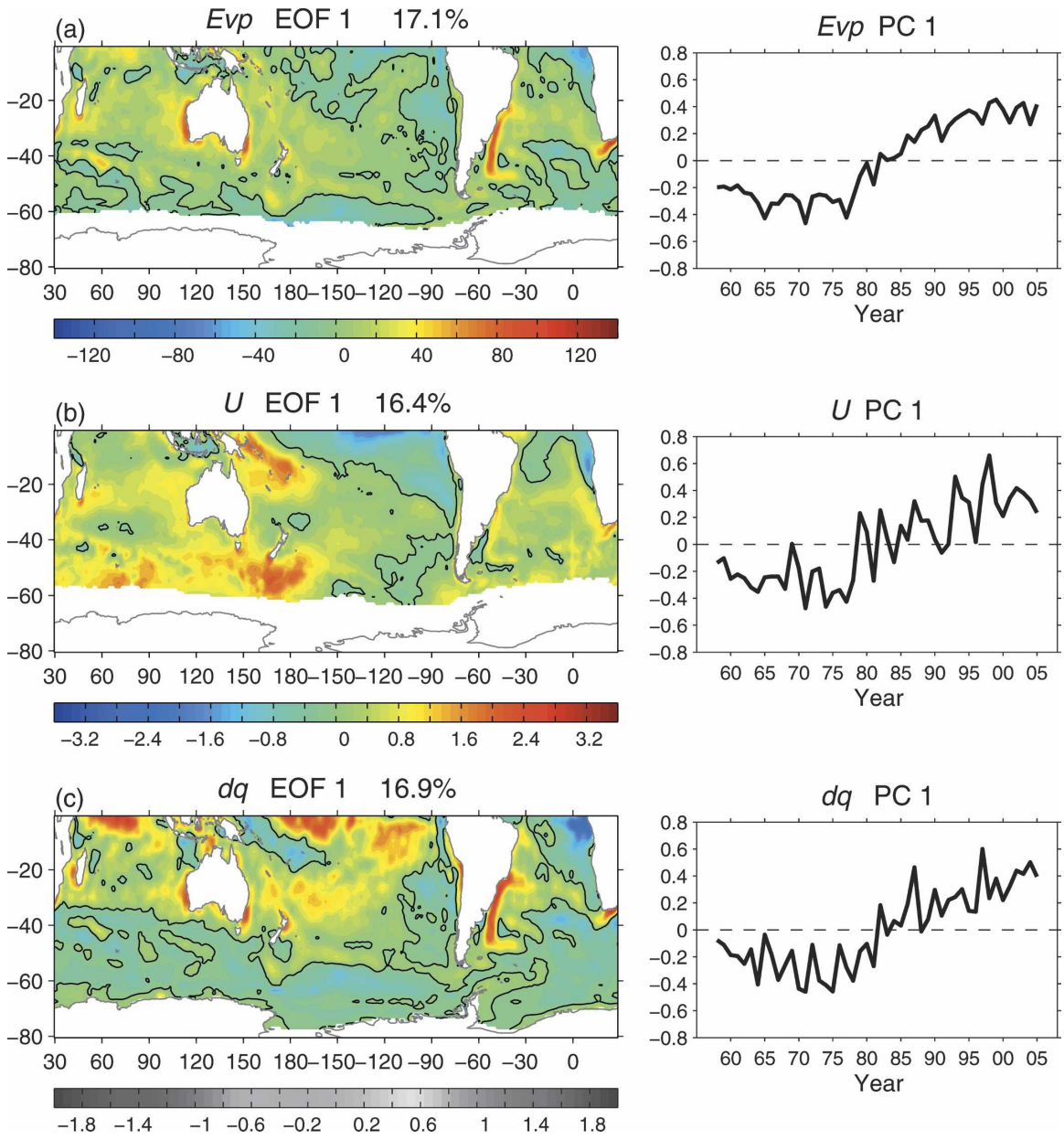

FIG. 9. Same as in Fig. 7, but for the yearly austral winter mean (June–August).

role of enhanced wind forcing in the decadal change of Evp and *dq*. It is hence hypothesized that wind impacts Evp by two ways. The processes are summarized by a schematic diagram shown in Fig. 12. In essence, the first way is direct: the greater wind speed induces more evaporation by carrying water vapor away from the evaporating surface to allow the air–sea humidity gradients to be reestablished at a faster pace. The second way is indirect: the enhanced surface wind strengthens the wind-driven subtropical gyre, which in turn drives a greater heat transport by the western boundary currents, warms up SST along the paths of the currents and extensions, and causes more evaporation by enlarging the air–sea humidity gradients.

It should be noted that, although Fig. 12 offers an explanation on the direct and indirect ways through which increased *U* drives up Evp, the fundamental factor that causes the upward trends in *U*, *dq*, and Evp since the late 1970s may well be SST. Yu and Weller (2007) analyzed the trend relationship between latent evaporation and SST using the OAFlux products. They found that the linear trend patterns in the two variables

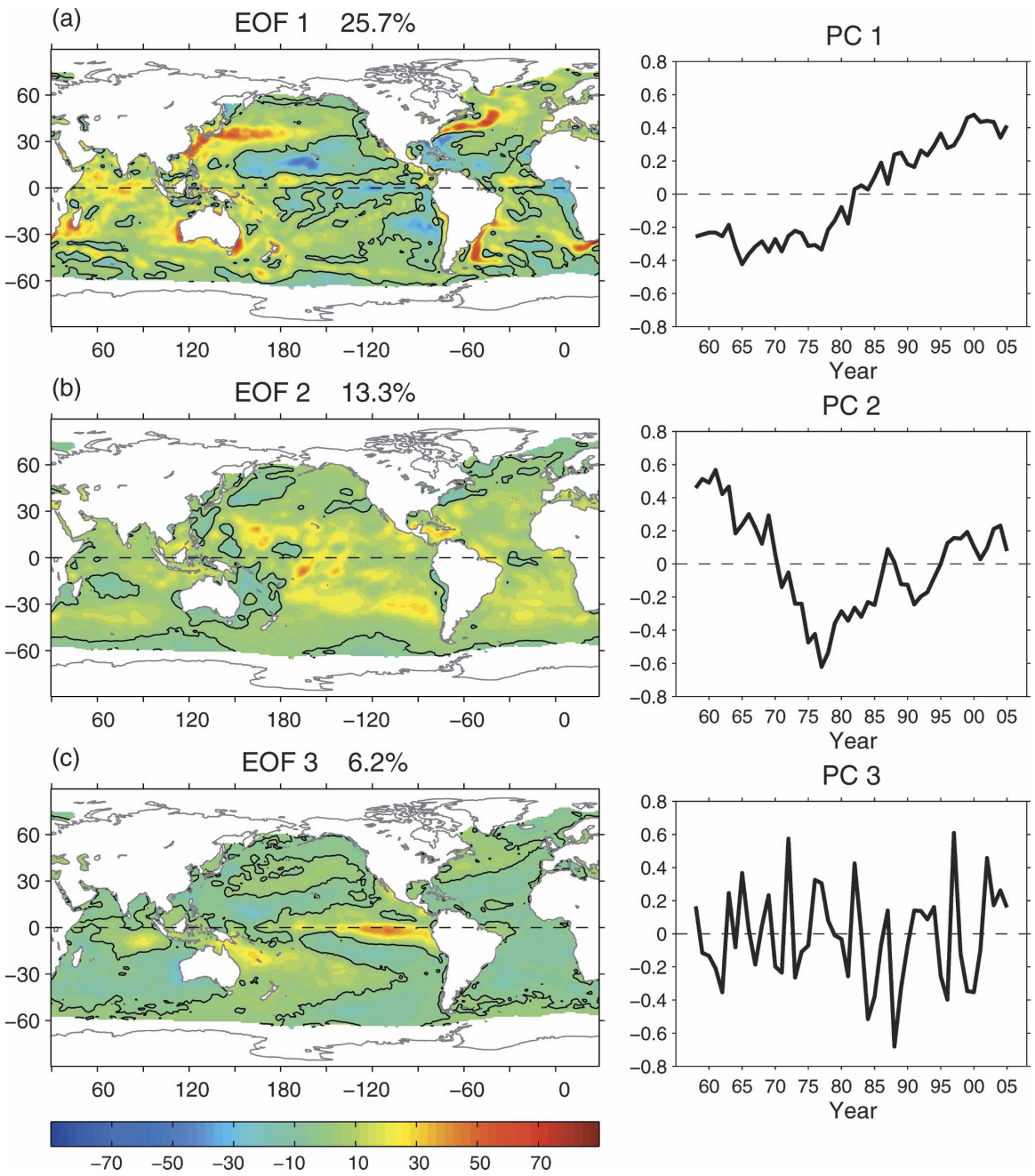

FIG. 10. (left) Pattern and (right) time series of the principal component for EOF (a) mode 1, (b) mode 2, and (c) mode 3 based on the yearly mean Evp fields for the period of 1958–2005. Zero contours are marked by black lines.

are very similar, suggestive of the atmospheric response to oceanic forcing. They also found that positive (negative) dq trends are in good agreement with positive (negative) LHF trends, indicative of the close connection between LHF and SST via dq. The explanation is that SST affects Δq, because SST not only determines q_s but also modulates the large-scale structure of q_a. By comparison, there is no well-defined local relationship between the trends in U and LHF. This does not mean that U is not important; on the contrary, U boosts the change in dq by carrying water vapor away from the evaporating surface and allowing dq to be reestablished at a fast pace. Ultimately, a nonzero dq, not U, is prerequisite for evaporation to occur. The analysis of Yu

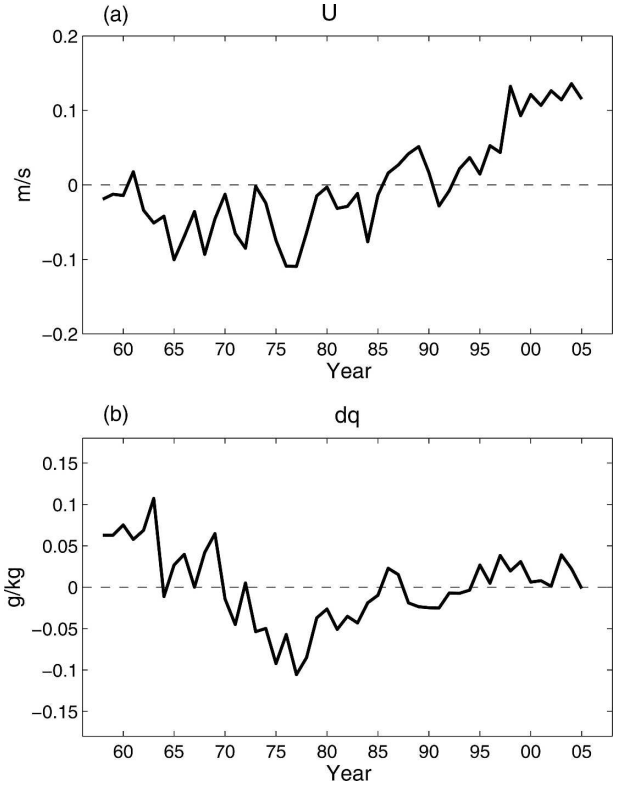

FIG. 11. Time series of yearly-mean (a) wind speed and (b) sea-air humidity differences averaged over the global ice-free oceans. The long-term mean over the period of 1958–2005 is removed.

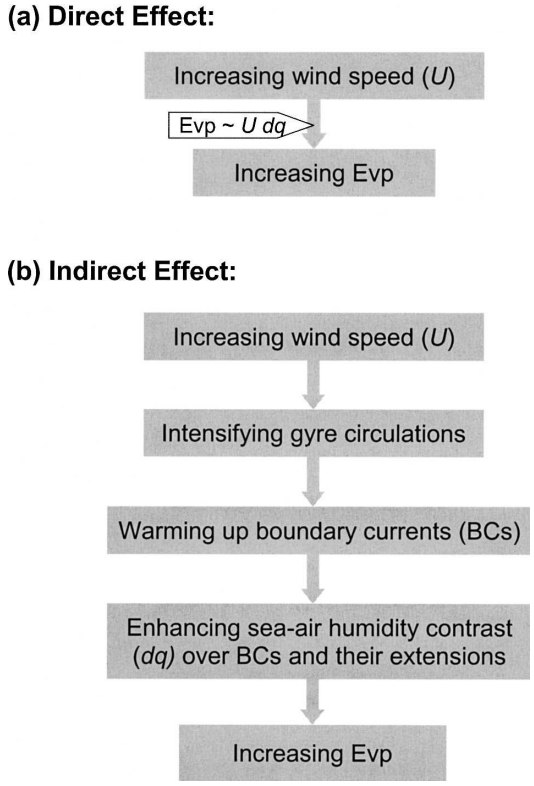

FIG. 12. Schematic diagram of the (a) direct and (b) indirect effects of increasing wind speed (U) on evaporation (Evp).

and Weller (2007) reinforced the notion that the relationship between Evp, U, and dq is nonlinear and that SST is a forcing for changes in evaporation.

The EOF analysis performed for the time series of the global annual-mean Evp fields provide an integrated view of dominant mode variability of the global Evp. The first three EOF modes account for nearly 50% of the total variance. The mode-1 variability represents the upward trend in Evp after 1980 and is induced primarily by increased U variability, while the mode-2 variability explains much of the downward trend in Evp before 1977–78 and is attributable to the global dq variability. The EOF mode 3 of Evp represents the interannual variability of Evp on time scales of ENSO, with the center of action primarily over the eastern equatorial Pacific.

The ocean, being the source of 86% of the global evaporation and the receiver of 78% of global precipitation (Schmitt and Wijffels 1993), is a key component of the global water cycle. An enhanced global oceanic Evp implies a changing global water cycle. The impact of the hydrologic cycle in the ocean is best seen in seawater salinity variations. A hydrographic data-based study by Curry et al. (2003) presented evidence of salinity increase in the northern and southern subtropics of the Atlantic Ocean between the 1950s and the 1990s, suggesting a 5%–10% increase in net evaporation (i.e., evaporation minus precipitation). The estimated 10% increase in the global Evp was based on the evaporation over the global oceans from the minimum in 1977–78 to the maximum in 2003. A better consistency can be expected if the estimation is made for the same period and same basin with the change of precipitation taken into consideration. It should be noted that there is generally no local relationship between changes in Evp and salinity, because salinity affects density and the latter modulates the ocean circulation that in turn redistributes salinity anomalies. However, the overall latitudinal changes in salinity should reflect the change of the hydrological cycle even if the local correlation is difficult to define.

At the same time, the increased amount of water vapor would cause an increase in the atmospheric moisture content. Recent satellite observations of the column-integrated water vapor (precipitable water) from SSM/I (Wentz and Schabel 2000; Trenberth et al. 2005) showed that atmospheric moisture amounts have been rising since the beginning of the data record in 1988.

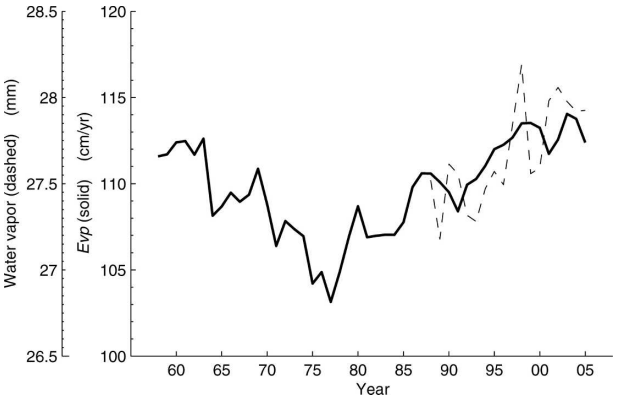

FIG. 13. Time series of the yearly mean SSM/I column-integrated water vapor averaged over the global oceans (solid) superimposed onto the time series of the yearly mean global oceanic evaporation (dashed).

When the yearly mean SSM/I observations of the column-integrated water vapor over the global oceans is superimposed onto the yearly mean time series of the global oceanic Evp (Fig. 13), it is clear that the upward tendencies of the two curves have good consistency despite large interannual signals. Pan evaporation measurements on land showed a declining evaporation trend over the past several decades, even though air temperatures have been increasing (Roderick and Farquhar 2002). The implication of Fig. 13 is that the oceans are likely the sole contributor to the increased atmospheric moisture content. If so, what are the implications to the global hydrological cycle and the precipitation patterns? Is there a strengthening of the hydrological cycle?

Acknowledgments. The author acknowledges the supporting grants from the NOAA Office of Climate Observations (OCO) and Climate Change Data and Detection (CCDD) and from the NASA Ocean Vector Wind Science Team. Bob Weller is sincerely thanked for helpful discussions. Xiangze Jin provided programming support for the OAFlux data products. SSM/I and satellite wind observations were provided by Frank Wentz and his Remote Sensing Systems Company from the website at http://www.ssmi.com. Information on the WHOI OAFlux project and related products can be found at http://oaflux.whoi.edu/.

REFERENCES

Barnett, T. P., 1984: Interaction of the monsoon and Pacific trade wind system at interannual time scales. Part II: The tropical band. *Mon. Wea. Rev.,* **112,** 2380–2387.

Bingham, F. M., 1992: Formation and spreading of subtropical mode water in the North Pacific. *J. Geophys. Res.,* **97,** 11 177–11 189.

Boyer, T. P., S. Levitus, J. I. Antonov, R. A. Locarnini, and H. E. Garcia, 2005: Linear trends in salinity for the World Ocean, 1955–1998. *Geophys. Res. Lett.,* **32,** L01604, doi:10.1029/2004GL021791.

Bradley, E. F., C. W. Fairall, J. E. Hare, and A. A. Grachev, 2000: An old and improved bulk algorithm for air–sea fluxes: COARE2.6a. Preprints, *14th Symp. on Boundary Layers and Turbulence,* Aspen, CO, Amer. Meteor. Soc., 294–296.

Bunker, A. F., 1976: Computations of surface energy flux and annual air–sea interaction cycles of the North Atlantic Ocean. *Mon. Wea. Rev.,* **104,** 1122–1140.

Cayan, D. R., 1992: Latent and sensible heat flux anomalies over the northern oceans: The connection to monthly atmospheric circulation. *J. Climate,* **5,** 354–369.

Chelton, D. B., and F. J. Wentz, 2005: Global microwave satellite observations of sea surface temperature for numerical weather prediction and climate research. *Bull. Amer. Meteor. Soc.,* **86,** 1097–1115.

Curry, R., B. Dickson, and I. Yashayaev, 2003: A change in the freshwater balance of the Atlantic Ocean over the past four decades. *Nature,* **426,** 826–829.

Daley, R., 1991: *Atmospheric Data Analysis*. Cambridge University Press, 457 pp.

da Silva, A. M., C. C. Young, and S. Levitus, 1994: *Anomalies of Heat and Momentum Fluxes.* Vol. 3, *Atlas of Surface Marine Data,* NOAA Atlas NESDIS 8, 413 pp.

Deser, C., M. A. Alexander, and M. S. Timlin, 1999: Evidence for a wind-driven intensification of the Kuroshio Current Extension from the 1970s to the 1980s. *J. Climate,* **12,** 1697–1706.

Esbensen, S. K., and V. Kushnir, 1981: The heat budget of the global oceans: An atlas based on estimates from marine surface observations. Oregon State University Climate Research Institute Rep. 29, 27 pp.

Fairall, C. W., E. F. Bradley, D. P. Rogers, J. B. Edson, and G. S. Young, 1996: Bulk parameterization of air-sea fluxes for Tropical Ocean-Global Atmosphere Coupled-Ocean Atmosphere Response Experiment. *J. Geophys. Res.,* **101,** 3747–3764.

——, ——, J. E. Hare, A. A. Grachev, and J. B. Edson, 2003: Bulk parameterization of air–sea fluxes: Updates and verification for the COARE algorithm. *J. Climate,* **16,** 571–591.

Houghton, J. T., Y. Ding, D. J. Griggs, M. Noguer, P. J. van der Linden, X. Dai, K. Maskell, and C. A. Johnson, Eds., 2001: *Climate Change 2001: The Scientific Basis*. Cambridge University Press, 881 pp.

Hurrell, J. W., 1995: Decadal trends in the North Atlantic Oscillation: Regional temperatures and precipitation. *Science,* **269,** 676–679.

Josey, S. A., E. C. Kent, and P. K. Taylor, 1999: New insights into the ocean heat budget closure problem from analysis of the SOC air–sea flux climatology. *J. Climate,* **12,** 2856–2880.

Kalnay, E., and Coauthors, 1996: The NCEP/NCAR 40-Year Reanalysis Project. *Bull. Amer. Meteor. Soc.,* **77,** 437–471.

Kanamitsu, M., W. Ebisuzaki, J. Woolen, J. Potter, and M. Fiorino, 2000: An overview of NCEP/DOE Reanalysis-2. *Proc. Second Int. Conf. on Reanalyses,* Reading, United Kingdom, WMO, 1–4.

Kelly, K. A., and S. Dong, 2004: The relationship of western boundary current heat transport and storage to mid-latitude ocean-atmosphere interaction. *Earth's Climate: The Ocean-*

Atmosphere Interaction, Geophys. Monogr., Vol. 147, Amer. Geophys. Union, 347–363.

Liu, W. T., K. B. Katsaros, and J. A. Businger, 1979: Bulk parameterization of air–sea exchanges of heat and water vapor including the molecular constraints at the interface. *J. Atmos. Sci.,* **36,** 1722–1735.

Mantua, N. J., S. R. Hare, Y. Zhang, J. M. Wallace, and R. C. Francis, 1997: A Pacific interdecadal climate oscillation with impacts on salmon production. *Bull. Amer. Meteor. Soc.,* **78,** 1069–1079.

McPhaden, M. J., and Coauthors, 1998: The Tropical Ocean-Global Atmosphere observing system: A decade of progress. *J. Geophys. Res.,* **103,** 14 169–14 240.

Miller, A. J., D. R. Cayan, and W. B. White, 1998: A westward-intensified decadal change in the North Pacific thermocline and gyre-scale circulation. *J. Climate,* **11,** 3112–3127.

Moyer, K. A., and R. A. Weller, 1997: Observations of surface forcing from the Subduction Experiment: A comparison with global model products and climatological datasets. *J. Climate,* **10,** 2725–2742.

Nakamura, H., G. Lin, and T. Yamagata, 1997: Decadal climate variability in the North Pacific during the recent decades. *Bull. Amer. Meteor. Soc.,* **78,** 2215–2225.

Oberhuber, J. M., 1988: An atlas based on the 'COADS' data set: The budgets of heat, buoyancy and turbulent kinetic energy at the surface of the global ocean. Max-Planck-Institut für Meteorologie Rep. 15, Hamburg, Germany, 20 pp. plus figures.

Qiu, B., and T. M. Joyce, 1992: Interannual variability in the mid- and low-latitude western North Pacific. *J. Phys. Oceanogr.,* **22,** 1062–1079.

Reynolds, R. W., T. M. Smith, C. Liu, D. B. Chelton, K. S. Casey, and M. G. Schlax, 2007: Daily high-resolution blended analyses for sea surface temperature. *J. Climate,* in press.

Roderick, M. L., and G. D. Farquhar, 2002: The cause of decreased pan evaporation over the past 50 years. *Science,* **298,** 1410–1411.

Roemmich, D., J. Gilson, R. Davis, P. Sutton, S. Wijffels, and S. Riser, 2007: Decadal spinup of the South Pacific subtropical gyre. *J. Phys. Oceanogr.,* **37,** 162–173.

Ross, R. J., and W. P. Elliott, 2001: Radiosonde-based Northern Hemisphere tropospheric water vapor trends. *J. Climate,* **14,** 1602–1612.

Schmitt, R. W., and S. E. Wijffels, 1993: The role of the oceans in the global water cycle. *The Legacy of Hann, Geophys. Monogr.,* Vol. 75, Amer. Geophys. Union, 77–84.

Servain, J., A. J. Busalacchi, M. J. McPhaden, A. D. Moura, G. Reverdin, M. Vianna, and S. E. Zebiak, 1998: A Pilot Research Moored Array in the Tropical Atlantic (PIRATA). *Bull. Amer. Meteor. Soc.,* **79,** 2019–2031.

Trenberth, K. E., 1990: Recent observed interdecadal climate changes in the Northern Hemisphere. *Bull. Amer. Meteor. Soc.,* **71,** 988–993.

——, J. Fasullo, and L. Smith, 2005: Trends and variability in column-integrated atmospheric water vapor. *Climate Dyn.,* **24,** 741–758.

Uppala, S. M., and Coauthors, 2005: The ERA-40 re-analysis. *Quart. J. Roy. Meteor. Soc.,* **131,** 2961–3012.

Vincent, D. G., 1994: The South Pacific Convergence Zone (SPCZ): A review. *Mon. Wea. Rev.,* **122,** 1949–1970.

Wentz, F. J., 1997: A well-calibrated ocean algorithm for SSM/I. *J. Geophys. Res.,* **102,** 8703–8718.

——, and M. Schabel, 2000: Precise climate monitoring using complementary satellite data sets. *Nature,* **403,** 414–416.

Yu, L., and R. A. Weller, 2007: Objectively analyzed air–sea heat fluxes for the global ice-free oceans (1981–2005). *Bull. Amer. Meteor. Soc.,* **88,** 527–539.

——, ——, and B. Sun, 2004a: Improving latent and sensible heat flux estimates for the Atlantic Ocean (1988–99) by a synthesis approach. *J. Climate,* **17,** 373–393.

——, ——, and ——, 2004b: Mean and variability of the WHOI daily latent and sensible heat fluxes at in situ flux measurement sites in the Atlantic Ocean. *J. Climate,* **17,** 2096–2118.

Zhang, G.-J., and M. J. McPhaden, 1995: The relationship between sea surface temperature and latent heat flux in the equatorial Pacific. *J. Climate,* **8,** 589–605.